TECHNICAL ARTICLE

Effect of Epoxy Sealant Loaded with Modified Montmorillonite on the Corrosion Resistance of Fe-Based Amorphous Metallic Coating

M.M. Liu, H.X. Hu, Z.B. Wang, S.L. Wu, and Y.G. Zheng

An epoxy resin loaded with modified montmorillonite (OMMT) was successfully employed to seal a Fe-based amorphous metallic coating (AMC). The OMMT was prepared by first modifying octadecylamine followed by intercalation with 2-mercaptobenzimidazole (MBI). The corrosion resistance of the as-prepared and as-sealed Fe-based AMCs was investigated by electrochemical impedance spectroscopy and salt spray tests. The results show that the sealing treatment using the OMMT-loaded epoxy can enhance the corrosion resistance of the Fe-based AMC, and the improvement is attributed to the combined effects of the high shielding ability originating from the epoxy sealant incorporated with the thin-layer-structured OMMT and the inhibition role of MBI which is released from the OMMT interlayer.

List of Symbols

MT	Montmorillonite
MBI	2-Mercaptobenzimidazole
MMT	MT modified by octadecylamine
OMMT	MT modified by octadecylamine and then intercalated with MBI
unsealed coating	Fe-based AMC
BE-sealed coating	Fe-based AMC sealed with blank epoxy
OE-sealed coating	Fe-based AMC sealed with OMMT-loaded epoxy
BE coating	The substrate directly sealed with blank epoxy, except for Fe-based AMC
OE coating	The substrate directly sealed with OMMT-loaded epoxy, except for Fe-based AMC
SBE-sealed coating	The excess sealant on the BE-sealed coating surface was not removed
SOE-sealed coating	The excess sealant on the OE-sealed coating surface was not removed

1. Introduction

High-velocity oxy-fuel (HVOF)-sprayed Fe-based amorphous metallic coatings (AMCs) have shown potential applications as surface protection coatings due to their good abrasive wear and corrosion resistance (Ref 1, 2). However, coating defects such as pores and microcracks are inevitably introduced during thermal spraying, and they directly influence the service lives of the coated substrate materials. Zhang et al. (Ref 3) provided direct evidence that the steel beneath the Fe-based AMC was preferentially corroded due to the presence of through-pores. They (Ref 4) also pointed out that the lower the coating porosity, the better the corresponding corrosion resistance. Therefore, the corrosion resistance of coatings can be improved by minimizing the existence of structural defects. Sealing treatment is a common and effective approach to reducing coating defects (Ref 5-7). The correlation between sealing treatment and the corrosion resistance of Fe-based AMCs has been studied by some researchers (Ref 8-12). Wang et al. (Ref 13) reported the effectiveness of three (AlPO$_4$, Na$_3$SiO$_4$, and cerium salt) sealing treatments in enhancing the

M.M. Liu, Normal College, Shenyang University, 54 Lianhe Road, Shenyang 110044, People's Republic of China; **H.X. Hu, Z.B. Wang,** and **Y.G. Zheng**, CAS Key Laboratory of Nuclear Materials and Safety Assessment, Institute of Metal Research, Chinese Academy of Sciences, 62 Wencui Road, Shenyang 110016, People's Republic of China; **S.L. Wu**, Jiangsu Special Equipment Safety Supervision & Inspection Institute, Changzhou Branch, 2180 Longcheng Road, Changzhou 213000, People's Republic of China. Contact e-mails: hxhu@imr.ac.cn and zbwang12s@imr.ac.cn.

corrosion resistance of a Fe-based AMC. However, most inorganic sealing processes are performed under heat treatments, and this limits their practical applications, while temperature limitations are not associated with organic sealants, hence they enjoy large-scale on-site constructions at room temperature.

A few reports have demonstrated the improvements of the corrosion resistance of coatings by epoxy sealing (Ref 9, 14). However, in many cases, the organic sealed layers remain permeable to corrosive species, such as dissolved oxygen and corrosive ions (Ref 15-17). To solve this, the incorporation of fillers, such as extenders and inorganic pigments, into the organic matrices can effectively decrease the diffusion paths of the corrosive media and enhance the anti-corrosion properties of the coatings (Ref 18-20). Among the various existing fillers,

montmorillonite (denoted as MT in this work) is a unique filler material due to its layer structure. Its main structural unit is composed of a layer of octahedral alumina sandwiched by two layers of the silicon-oxygen tetrahedron. This special layer structure endows MT with its unique properties, such as ion exchange and swelling. Thus, the fabrication of a Fe-based AMC with MT-loaded epoxy offers promising prospects for improving the corrosion resistance of the coating.

In addition, the incorporation of corrosion inhibitors into sealants has been demonstrated to be an effective way of endowing coatings with self-healing properties (Ref 21, 22). Moon et al. (Ref 21), Mohedano et al. (Ref 22), and Laleh et al. (Ref 23) proved that the corrosion resistances of their respective coatings were improved by cerium-based sealing treatments. A contradictory view holds that the direct addition of corrosion inhibitors to sealants usually affects their cross-linking reactions, thereby deteriorating the protective performances of the sealed layers (Ref 8). The use of corrosion inhibitor-loaded nanocontainers does not only overcome the detrimental effects associated with direct inhibitor additions, but also ensures the release of the corrosion inhibitors on demand (Ref 24-32). MT has been previously applied as a nanocontainer for corrosion inhibitors (Ref 26, 33). Ghazi et al. (Ref 34) studied the corrosion protection property of benzimidazole (BIA) and zinc cations (Zn^{2+}) intercalated MT and found that the efficient protection ability of the material resulted from the combined effects of the BIA^+ and Zn^{2+} cations. The study also provided a novel idea for the introduction of corrosion inhibitors into MT, which is expected to endow sealed layers with certain self-healing properties.

The main objective of this work is to develop a dual-purpose sealed coating with excellent barrier properties and active corrosion protection abilities. MT was first modified by octadecylamine and intercalated with 2-mercaptobenzimidazole (OMMT). Then, the epoxy sealant loaded with OMMT was applied to a Fe-based AMC. The morphology and structural characterization of MT before and after treatment were studied by SEM, FTIR, TGA, and XRD. The release kinetics of MBI from the OMMT interlayer was performed by UV spectroscopy. The influence of sealing treatment on the corrosion resistance of the Fe-based AMC was investigated by electrochemical impedance spectroscopy (EIS) and salt spray test. Additionally, the corrosion protection mechanism was proposed and discussed in details.

2. Experimental

2.1 Materials

The HVOF-sprayed Fe-based AMC used in this work had the following composition in wt. %: Fe: 54.2, Cr: 18.3, Mo: 13.7, Mn: 2.0, W: 6.0, B: 3.3, C: 1.1, Si: 1.4. The powder was produced by argon atomization at a dynamic pressure of 7 MPa after heating to 1600 K, and the as-atomized powder with the particle sizes of 15-45 μm were sprayed on the substrate (10CrNi3MoV carbon steel). The spraying parameters were as follows: the oxygen flow, kerosene flow, and air flow were 252, 72, and 399 standard cubic feet, respectively; the spraying distance was 250 mm; the feed rate was 20 g/mm, and the traverse velocity was 800 mm/s (Ref 13, 35, 36). Epoxy resin was supplied by Kukdo chemical (Kunshan) co., Ltd. Mont-

morillonite (MT) was provided by Lingshou County Heng-chang Mineral Processing Factory and used as received without further purification. Octadecylamine and 2-mercaptobenzimidazole (MBI) were of analytical reagent grade purchased from Sinopharm Chemical Reagent Co., Ltd.

2.2 Preparation of OMMT

OMMT was prepared by a two-step process. Firstly, 20 g of MT was dissolved in 1800 mL of deionized water and magnetically stirred for 12 h at room temperature. Then, 96.8 mM/L of octadecylamine and deionized water (pH = 3-4) were gradually added to the above solution under vigorous stirring, followed by a reaction at 80 °C for 24 h, wherein pH was adjusted with dilute hydrochloric acid. After that, the suspended powder was prepared, centrifuged, and rinsed in a water/ethanol solution and then centrifuged again until no AgCl precipitate was formed in the residual solution, which was designated as MMT.

Secondly, MMT was used as a nanoreservoir for corrosion inhibitors. Supersaturated MBI was dissolved in a mixture of MMT, acetone, and water, then transferred to vacuum equipment (2×10^3 Pa) which was maintained at room temperature for 3 h. Afterwards, the precipitate was washed with distilled water, followed by ethanol to remove the excess corrosion inhibitor. Finally, the prepared powder was dried overnight at 60 °C, ground to pass through a 200-mesh sieve, and denoted as OMMT.

2.3 Preparation of Fe-Based AMC Sealed with OMMT-Loaded Epoxy

The epoxy sealant doped with OMMT was applied on the Fe-based AMC (OE-sealed coating) using a film applicator, and then cured for 2 h at 100 °C (Viscosity: $\leq 43.1 \pm 0.8$ mPa·s, Brookfield DV-III + Rheometer, USA). By comparison, the Fe-based AMCs sealed with and without blank epoxy resin are addressed as "BE-sealed coating" and "unsealed coating", respectively, in the following discussion. The penetration depth of the blank epoxy sealant and the epoxy loaded with OMMT was approximately 380 and 370 μm for BE-sealed coating and OE-sealed coating. The excess sealant (45 ± 2 μm) on the surface of the sealed coatings used in the EIS test was ground with 1000-grit SiC paper, but was not removed in the salt spray test.

2.4 Characterization

2.4.1 The Morphology and Structure Characterization. The surface morphologies of the MT and OMMT powders, as well as the unsealed, BE-sealed and OE-sealed coatings were observed by scanning electron microscopy (SEM, FEI-Inspect F) equipped with energy dispersive x-ray spectrometer (EDS). The treatment of the organic molecular chain on MT could have led to its chemical transformation from inorganic to organic, and this was examined by Fourier transform infrared spectroscopy (FTIR, Bruker IFS55). The FTIR spectra were obtained in KBr pellet and recorded in the wavenumber range of 4000-400 cm^{-1} with 4 cm^{-1} resolution. Thermogravimetric analysis was conducted with Thermo-gravimetry Analyzer SETSYS Evolution18 (SETARAM, France) in the range of 50-800 °C at a heating rate of 10 °C/min in a nitrogen atmosphere. Moreover, x-ray diffraction

(XRD) test was utilized to characterize the changes in the interlayer distance for MT, MMT, and OMMT. This was performed using a Rigaku D/max 2400 diffractometer (Tokyo, Japan) with monochromated Cu Ka radiation (λ = 0.1542 nm).

2.4.2 The Release Kinetics of MBI from the OMMT Interlayer. The release kinetics of MBI from the OMMT was carried out with UV-2100 spectrophotometer (Beijing Ruili Analytical Instruments Ltd.). To test the effect of solvent type and concentration on the release rate of MBI, 0.05 g OMMT was vigorously stirred in 1000 mL deionized water, 0.35 wt.% NaCl, and 3.5 wt.% NaCl, respectively. The solutions were stirred for a defined time and filtered. Afterwards, the concentrations of MBI in the filtrates were measured and the release profiles of MBI from the OMMT interlayer of the three solutions were calculated.

2.4.3 Corrosion Protection Performance Evaluation. The corrosion protection performances of the coatings were examined by electrochemical impedance spectroscopy (EIS) and salt spray test.

EIS test was conducted using a Potentiostat/Galvanostat (PARSTAT 2273). A classical three-electrode cell included the samples with exposed areas of 12.56 cm^2 (working electrode), saturated calomel electrode (SCE) (reference electrode), and platinum plate (counter electrode). EIS spectra were obtained at OCP using an amplitude signal voltage of 20 mV exposed to 0.35 wt.% NaCl solution in the frequency range from 100 kHz to 10 mHz. The corrosion rate of the coating was reduced at a low concentration of the corrosive media (0.35 wt.% NaCl), which was beneficial to the evaluation of the corrosion protection mechanism of MBI released from the OMMT interlayer for the OE-sealed coating, and it was also based on the results of MBI release kinetics. Moreover, a Faraday cage was used to minimize external interferences on the system during testing. The obtained EIS data were analyzed by the ZsimpWin software.

The long-term corrosion resistances of the coatings were evaluated by a neutral salt spray test (5 wt.% NaCl, pH: 6.5-7.2, temperature: 35 ± 1 °C) according to the standard ASTM B117. The samples were periodically taken out and their corrosion performances were evaluated during exposure.

2.4.4 Self-Healing Capability Evaluation. The epoxy sealants with (OE) and without (BE) OMMT were directly applied on the steel substrate, and not the Fe-based AMC, to estimate the inhibition effect of MBI on the substrate beneath the Fe-based AMC. With the aid of sharp metallic blade, an artificial defect with length 5 mm and width 0.75 ± 0.25 mm was made on the coating surfaces until the metal substrates beneath the sealants were exposed. After 6 h immersion, the morphologies and chemical compositions of the two coatings with artificial defects (Ref 34) were measured using an electron probe x-ray microanalyzer (Shimadzu Model EPMA-1610).

3. Results and Discussion

3.1 Effect of Surface Treatment on MT

To analyze the polarity of montmorillonite before (MT) and after (OMMT) treatment, and to assess the compatibility of OMMT with the organic phase, MT is added to deionized water, while OMMT is added to deionized water and ethanol. The dispersibility and stability of the powders in the different solvents are shown in Fig. 1. As observed in Fig. 1a, MT is fully dissolved in deionized water because of its water solubility. On the other hand, OMMT is insoluble in deionized water as it is observed to float on the surface (Fig. 1b), but it is homogeneously dispersed in ethanol (Fig. 1c). There are still no OMMT deposits found in the ethanol after one month. These results suggest that the polarity of the treated MT (OMMT) is transformed from hydrophilicity to hydrophobicity. Similarly, it is reasonable to draw an inference that OMMT is capable of being uniformly and stably dispersed in the epoxy sealant.

3.2 Morphology Characterization

Figure 2 depicts the SEM micrographs of MT and OMMT. As shown in Fig. 2a, MT displays a plate-like structure which is highly aggregated. The EDS result reveals the presence of carbon, oxygen, aluminum, and silicon in the MT structure. In contrast, an obvious change is observed in Fig. 2b where OMMT is exfoliated into a single layer of slices. According to EDS microanalysis, the spectrum presents a new S element derived from MBI in addition to all the elements characterized for MT, as well as a significantly higher concentration of C element (Fig. 2b1) compared to that shown in Fig. 2a1. The results demonstrate the intercalation of octadecylamine and MBI into the OMMT interlayer.

3.3 FTIR Test

Figure 3 shows the FTIR spectra of MT and OMMT. For the untreated MT (Fig. 3a), the peaks around 3624, 3450 and 1652 cm^{-1} are assigned to the stretching and bending vibrations of O–H on the MT surface (Ref 19, 26, 37). The bands around 1090 and 1039 cm^{-1} are ascribed to the stretching vibration of Si-O (Ref 19, 26, 38). Furthermore, the peaks around 621 and 519 cm^{-1} are ascribed to Al-O and Si–O bending vibrations (Ref 19, 26, 39). In the case of OMMT (Fig. 3b), the intensities of the bands around 3624 and 3450 cm^{-1} are weaker in comparison to those of the pristine MT, which implies that the modification has an effect on the structure of MT. Apart from the characteristic peaks of MT, the new absorption peaks at 2922 and 2850 cm^{-1} are attributed to the asymmetric and symmetric stretching vibrations of C-H, respectively (Ref 40), suggesting the presence of octadecylamine in the OMMT. The peaks around 1641, 1597, 1512, and 1468 cm^{-1} are derived from the C = C stretching vibration of benzene rings (Ref 41). Additionally, the multiple peaks from 3150-3000 cm^{-1} are ascribed to the stretching vibration of C-H from the benzene ring, while the sharp peak at 744 cm^{-1} is assigned to the out-plane bending vibration of C-H (Ref 42), indicating the presence of a 1, 2-disubstituted benzene ring structure in the compound. The peak at 2570 cm^{-1} is assigned to the stretching vibration of S-H. These results demonstrate the presence of MBI in the OMMT interlayer.

3.4 Thermogravimetric Analysis

Figure 4 shows the TGA diagrams of MT, MMT, and OMMT. There are two weight loss stages for MT (Fig. 4a). The first stage is observed at temperatures between 80 and 150 °C, and it is related to the desorption of physically absorbed water on MT. An additional weight loss is observed above 600 °C, which is attributed to the release of –OH from the MT lattice (Ref 34, 43). By contrast, MMT and OMMT display either
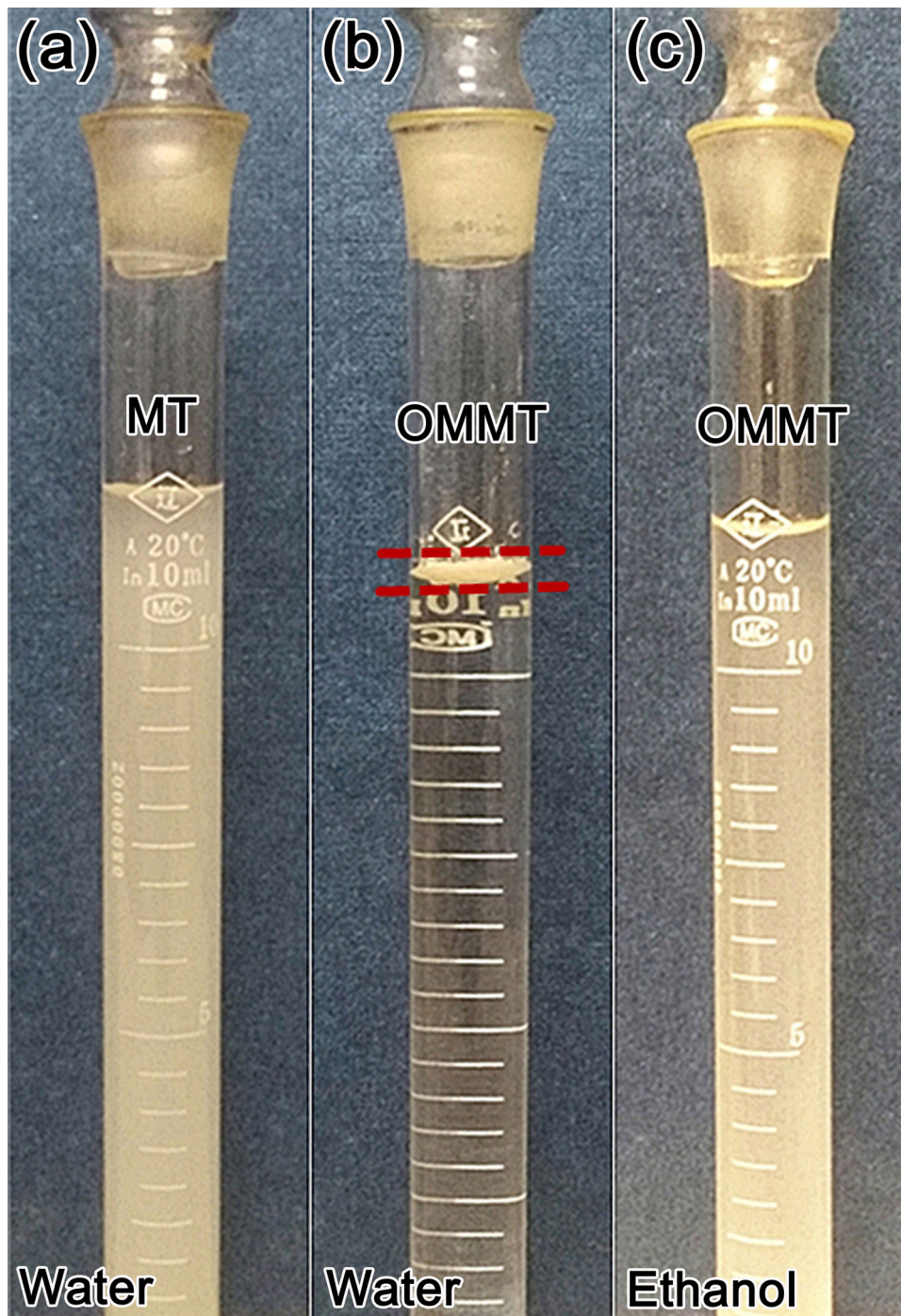
Fig. 1 The dissolution of montmorillonite before (MT) and after (OMMT) treatment in different solvents. (a) MT in deionized water; (b) OMMT in deionized water, and (c) OMMT in ethanol

small or no weight loss below 150 °C. For MMT, the second and third weight loss stages around 230 and 350 °C are attributed to the thermal decomposition of octadecylamine (b. p. 232 °C) on the MMT surface and its introduction into MMT, respectively. Moreover, the weight loss percentage is about 25% (Fig. 4b). For OMMT, it is observed that the second weight loss (about 31%) occurs around 300-500 °C (Fig. 4c). The removal of the long-chain octadecylamine grafting on the OMMT surface results to the disappearance of the thermal decomposition around 230 °C. Besides, the retardation of the degradation temperatures for octadecylamine (b. p. 232 °C) and MBI (b. p. 300-304 °C) inside the interlayer are caused by the barrier role of the OMMT plates. Note that the increase in weight loss for OMMT compared to MT (Fig. 4a) and MMT (Fig. 4b) signifies the successful incorporation of both the long-chain alkylamine and MBI into the OMMT gallery.
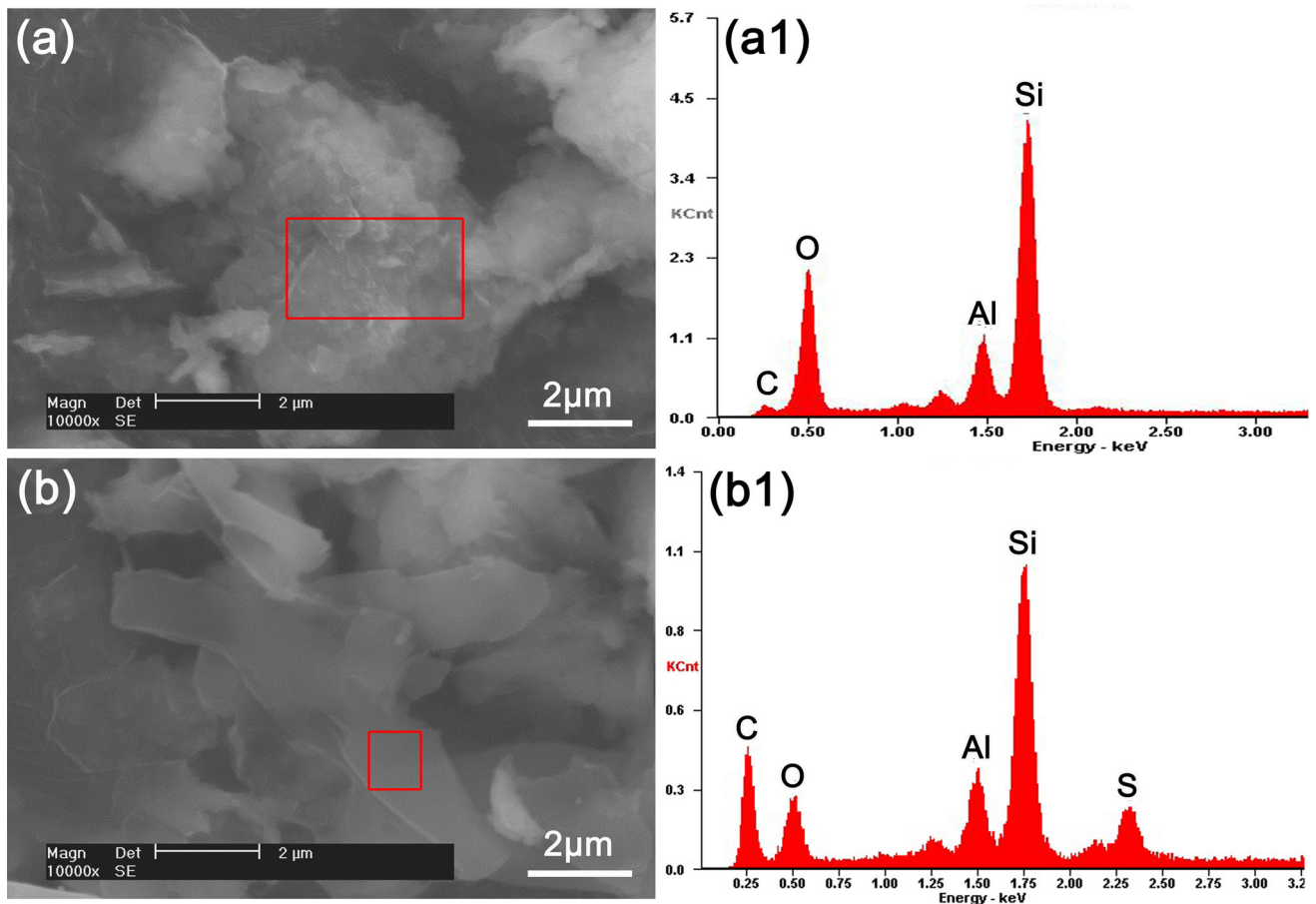
Fig. 2 SEM micrographs with EDS elemental analysis of (a), (a1) MT and (b), (b1) OMMT

3.5 X-ray Diffraction (XRD) Study

The XRD patterns of MT, MMT and OMMT are presented in Fig. 5, and the values of the basal spacing (d_{001}) are calculated based on Bragg's Law. According to Fig. 5, the diffraction peak (d_{001}) for MT appears around $2\theta = 7.09$, which corresponds to a layer d-spacing of 1.245 nm. Compared with MT, the basal spacing of MMT and OMMT increases from 1.245 to 1.846 nm ($2\theta = 4.78$) and 1.944 nm ($2\theta = 4.54$), respectively, indicating the successful intercalation of octade-cylamine ($CH_3(CH_2)_{17}NH_3^+$) and MBI into the MT gallery. Some references (Ref 34, 44) pointed out that the sizes and amounts of the intercalated species are responsible for the different heights of galleries. The length of the octadecylamine molecule is estimated to be around 23.97 Å (calculated by ACD/3D view), which is bigger than the interlayer distance of MMT (18.46 Å). This result indicates that $CH_3(CH_2)_{17}NH_3^+$ which is present in the clay interlayer is inclined at an angle of about 39.6°. On the other hand, the basal spacing of MMT is far larger than that of MBI (length: 8.67 Å, width: 5.34 Å), which is favorable for its further intercalation. The small difference in basal spacing between OMMT and MMT may be attributed to the introduction of MBI between the long-chain alkylamine groups. Correspondingly, the angle between $CH_3(CH_2)_{17}NH_3^+$ and the vertical line becomes smaller (about 35.8°).

3.6 Release Study

The absorbance values of the different concentrations of MBI in distilled water, 0.35 wt.% NaCl, and 3.5 wt.% NaCl are determined by measuring the characteristic peak of MBI at 242 nm (Fig. 6a), and the corresponding standard curves are presented in Fig. 6(b-d). According to Fig. 6(b-d), a linear relationship exists between the concentrations of MBI (C_i, $i = 1, 2, 3$) and the absorbance values (A_i, $i = 1, 2, 3$) in the three solvents, as follows:

$$A_1 = 0.1046C_1 + 0.0411 \tag{Eq 1}$$

$$A_2 = 0.1053C_2 + 0.0424 \tag{Eq 2}$$

$$A_3 = 0.1020C_3 + 0.0353 \tag{Eq 3}$$

where 1, 2 and 3 correspond to deionized water, 0.35 wt.% NaCl, and 3.5 wt.% NaCl, respectively.

To quantify the release kinetics of MBI, 0.05 g OMMT was first placed in a beaker with 1000 mL distilled water, 0.35 wt.% NaCl, and 3.5 wt.% NaCl, respectively. The solutions were vigorously stirred for a certain time and filtered. Then the absorbance values of MBI in the filtrates were measured at different mixing times and in different electrolyte solutions. The corresponding concentrations of MBI in the three elec-
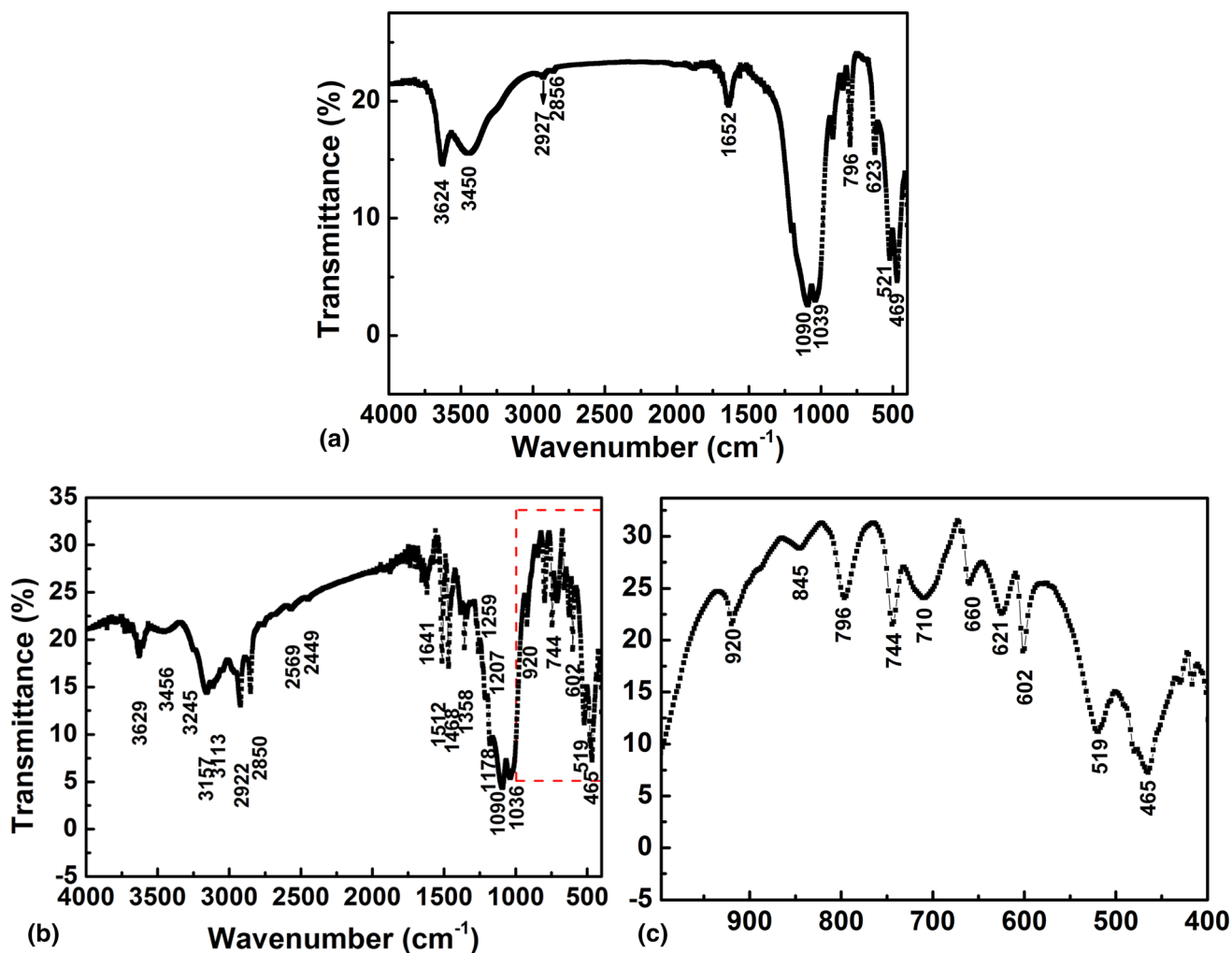
Fig. 3 FTIR spectra of (a) MT, (b) OMMT and (c) local higher magnification of (b)

trolytes are calculated based on Eq 1-3. Moreover, the loading amount of MBI inside the OMMT interlayer is also measured by UV analysis, and then the release percentage (%) of MBI in the different electrolyte solutions versus stirring time is calculated, as shown in Fig. 7.

As presented in Fig. 7(a) and (b), for deionized water and 0.35 wt.% NaCl, the release amount increases with stirring time. The release profile of MBI nearly reaches a plateau after 160 min (Fig. 7a) and 80 min (Fig. 7b), corresponding to 70.8 and 66.9% of the loaded capacity, respectively. The release rate of MBI in the NaCl solution (Fig. 7b) is much higher than that in deionized water (Fig. 7a) at the early stages (0-60 min). This is because NaCl is a strong electrolyte and can be rapidly ionized, thus it is capable of replacing MBI in the OMMT interlayer. In contrast, water is a weak electrolyte. For the same strong electrolyte (NaCl) but at different concentrations, the increase in concentration (from 0.35 to 3.5 wt.%) leads to a sharp increase in the amount of leached MBI. As expected, the maximum release reaches a plateau within only 5 min, where the percentage of released MBI is 89.3% (Fig. 7c). Based on these experimental results, it is reasonable to suggest that when the aggressive species penetrate the coating and attack the

substrate, the MBI in the OMMT interlayer is leached out and migrates to the corrosion sites, thus offering protection against corrosion.

3.7 EIS Test

Figure 8 presents the Nyquist and Bode plots of the unsealed, BE-sealed, and OE-sealed coatings immersed in 0.35 wt.% NaCl solution at different times. As shown in Fig. 8a, the radius of capacitance arc for the unsealed coating reduces sharply with increasing immersion time (0-24 h), indicating the fast degradation of the anti-corrosion ability of the Fe-based AMC. The radius of the capacitance arc and the impedance value at 0.01 Hz are observed to have increased from 96 to 216 h (Fig. 8a and b). In the case of the BE-sealed coating (Fig. 8c and d) and OE-sealed coating (Fig. 8e and f), the impedance values at 0.01 Hz are higher than that of the unsealed coating throughout the entire immersion. This indicates that the sealing treatment improves the corrosion resistance of the Fe-based AMC.

To better understand and analyze the degradation processes of the three coatings, the equivalent circuits depicted in Fig. 9
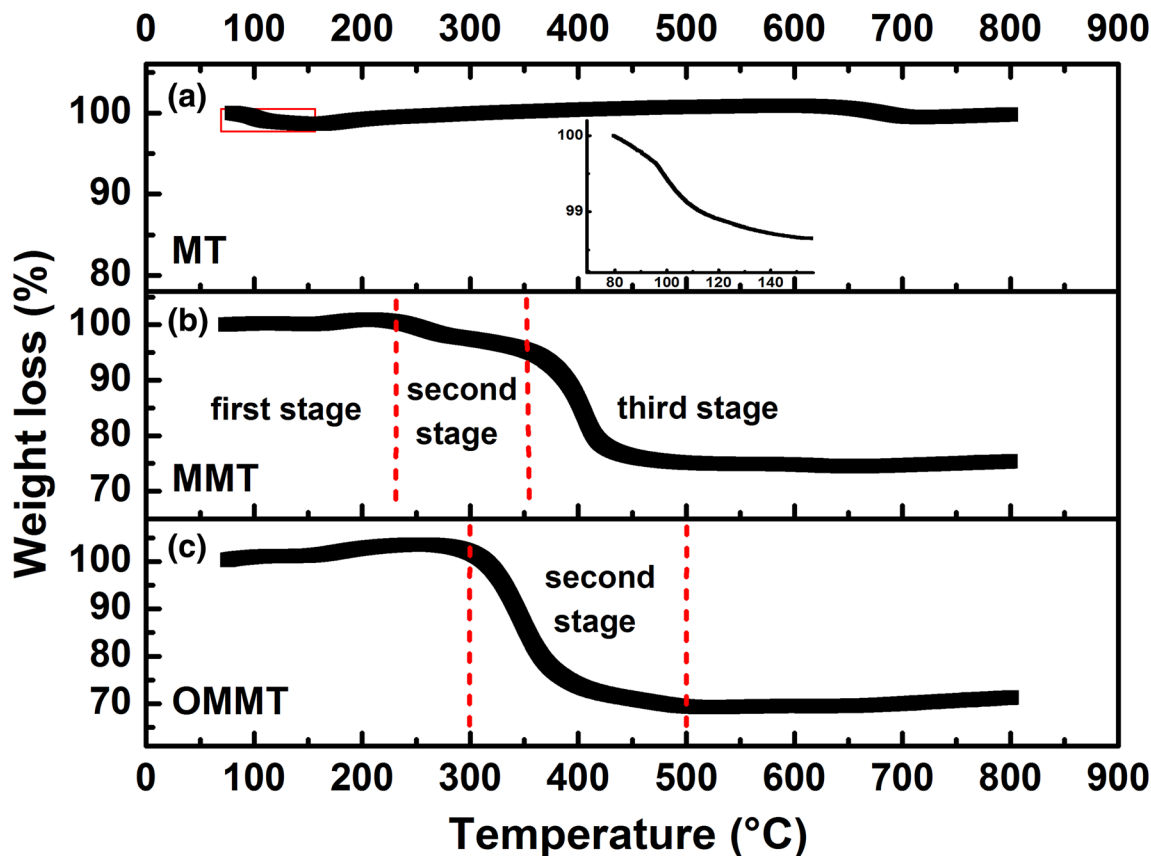
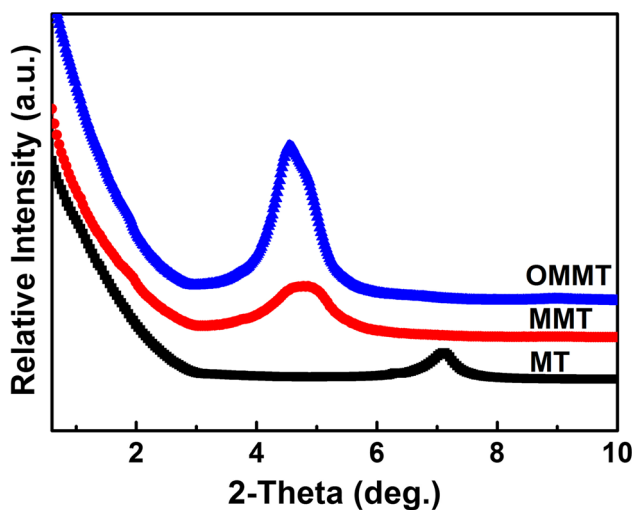**Fig. 4** TGA diagrams of (a) MT, (b) MMT and (c) OMMT

Fig. 5 XRD patterns of MT, MMT, and OMMT

are proposed to fit the EIS spectra based on the structural characteristics of the outer and inner layers of the coating and relevant references (Ref 9, 10, 12, 22, 45). When the amorphous coating is exposed to corrosive media, the solution can diffuse into the microcracks and pores in the outer layer of the coating to induce corrosion. Therefore, the equivalent circuit model A with two time constants shown in Fig. 9a is used to fit the 0-24 h EIS data of the unsealed coating. R_{out} is

assigned to the charge transfer resistance on the outer porous layer of the unsealed coating where the corrosion reaction occurs. R_{in} is the resistance of the inner lower porosity layer. While the charge transfer process detected in the micropores of the two sealed coatings is caused by incomplete sealing (Fig. 9b), R_{ct} is associated with the corrosion resistance within the micropores. R_c is the resistance of the sealed coatings. With prolonging the immersion (96-216 h), the charge transfer process is transferred to the surface of the substrate due to the penetration of corrosive media. For equivalent circuit model C as shown in Fig. 9c, three time constants are applied to simulate the EIS plots of the three coatings. The alternative third time constants of R_{ct} and Q_{dl} represent the polarization resistance and double-layer capacitance at the electrolyte/substrate interface. R_{out} and R_{in} are assigned to the resistance of the outer layer and the inner layer of the unsealed and sealed coatings, respectively. The equivalent circuit diagrams are well fitted to the corresponding EIS spectra, with chi-square values in a magnitude order of 10^{-3} (Ref 10).

Figure 10 displays the variations of total resistance R_{total} ($R_{total} = R_{out} + R_{in}/R_{out} + R_{in} + R_{ct}$) (Ref 22) for the three coatings versus immersion time. It is seen that the R_{total} of the unsealed coating drops sharply from 0 to 24 h due to the penetration of the corrosive solution. As observed in Fig. 11a and b, there are some pores and microcracks in the coating, which provide diffusion channels for the penetration of corrosive media. However, the R_{total} values of the other two sealed coatings exhibit ascending trends. This is because coating defects are minimized by the sealing treatment, and
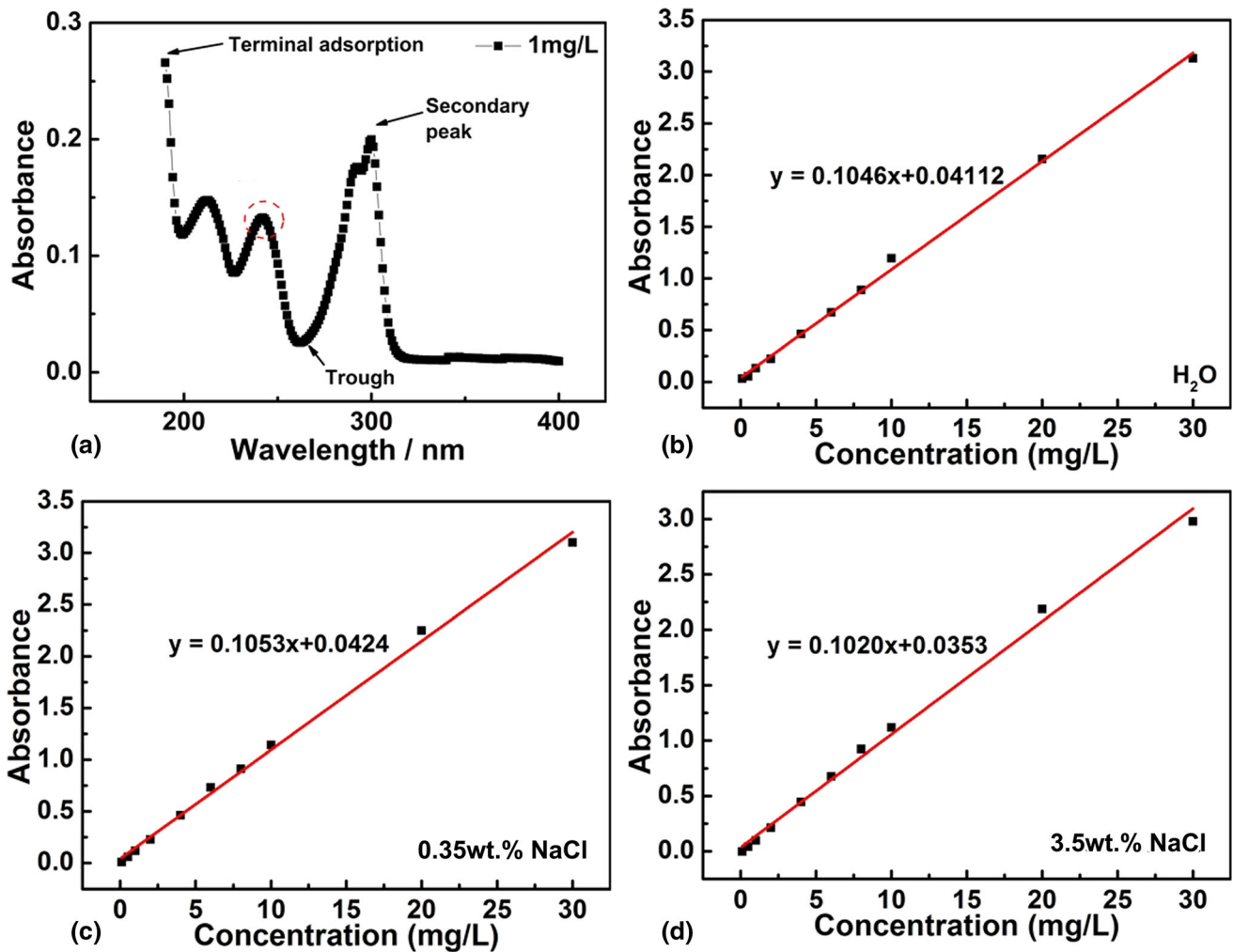
Fig. 6 (a) UV spectrum of MBI. The standard curves of different concentrations of MBI in (b) distilled water, (c) 0.35 wt.% NaCl and (d) 3.5 wt.% NaCl by measuring the characteristic peak of MBI at 242 nm

fewer structural defects in turn suppress the diffusion of electrolytes. Correspondingly, the BE-sealed and OE-sealed coatings are well sealed except for the microdefects generated during the curing process of the sealants (Fig. 11c-f). The unsealed coating exhibits a rapid increase in impedance towards the later stages of immersion (96-312 h). When the corrosive media reaches the coating/substrate interface, the substrate is polarized and acts as an anode to corrode, and the accumulation of corrosion products offers a degree of protection against further corrosion (Ref 3, 4, 46). For the BE-sealed coating, the R_{total} values are relatively stable from 96 to 168 h, and then decrease (168-312 h). This phenomenon may be related to the corrosion protection, and deterioration of the sealed layer, respectively. It is noteworthy that the R_{total} values of the OE-sealed coating show a slight increase and are higher than those of the other two coatings. The addition of OMMT with a layered structure into the epoxy sealant leads to the improvement of the physical barrier performance (Fig. 11e and

f). Moreover, the MBI released from the OMMT interlayer migrates to the active anodic sites to reduce the corrosion rate (Ref 32, 34).

3.8 Salt Spray Test

Generally, the excess sealant on a coated surface should be ground off before test, such as the samples in the electrochemical experiments of this study, as well as those from some research related to sealing treatments (Ref 10, 47). However, this is needless in practical applications. Combined with the actual situation, the excess sealants on the surface of the BE-sealed and OE-sealed coatings are not removed in the salt spray test, and the samples are denoted as "SBE-sealed coating" and "SOE-sealed coating", respectively.

Figure 12 illustrates the optical images of the unsealed, SBE-sealed, and SOE-sealed coatings after 48, 1000 and
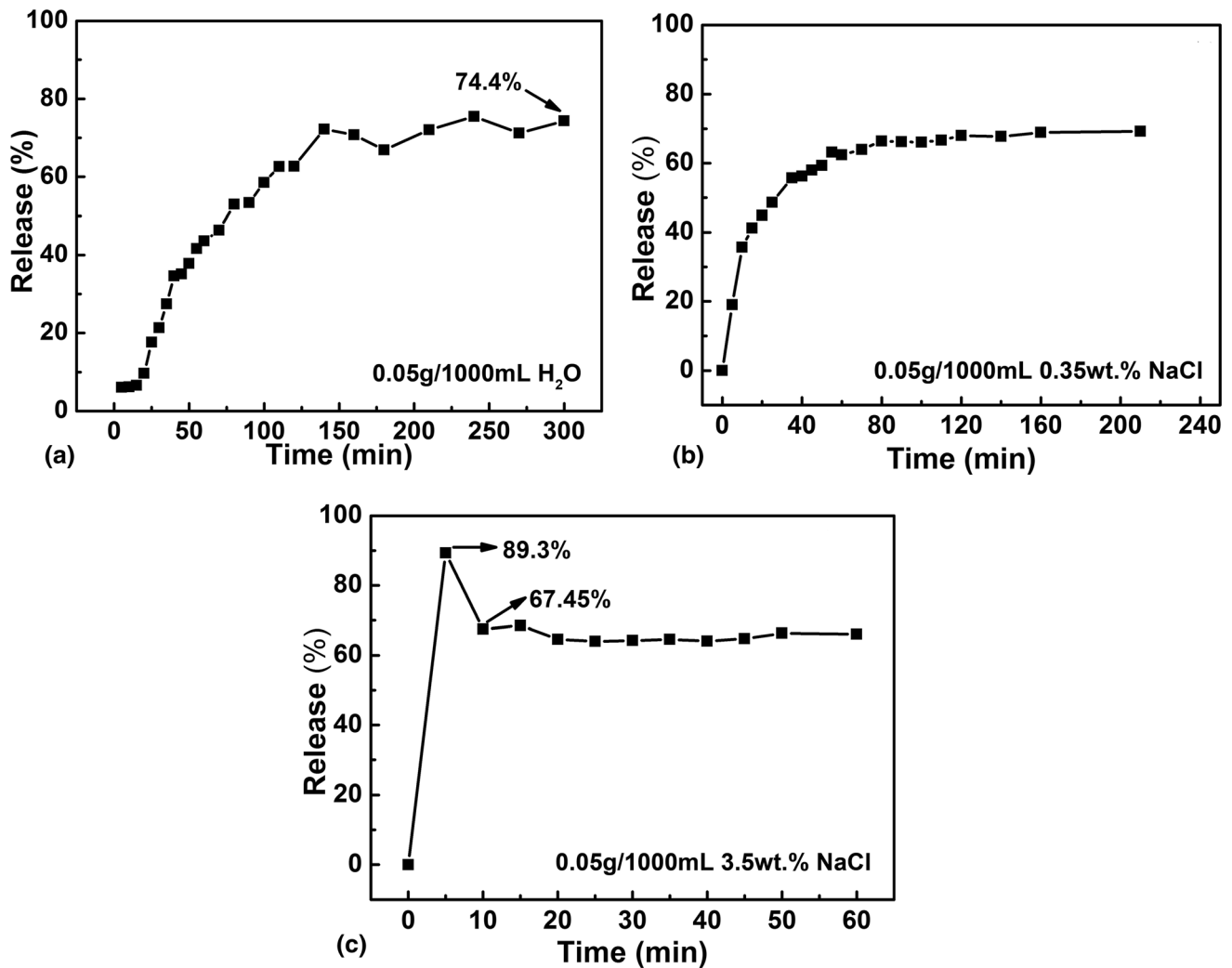
Fig. 7 Release kinetics of MBI from the OMMT interlayer into 1000 mL (a) deionized water, (b) 0.35 wt.% NaCl and (c) 3.5 wt.% NaCl

2000 h salt spray tests. Clearly, several corrosion spots are observed on the surface of the unsealed coating after exposure for only 48 h (Fig. 12a), indicating its poor corrosion protection ability. This is consistent with the EIS results (Fig. 8a and b). With prolonged exposure (1000 h), the entire surface of the unsealed coating is almost filled with corrosion products (Fig. 12d). This means that the unsealed coating is failed and could not protect the substrate from corrosion. However, there is no corrosion on the surface of the SBE-sealed coating (Fig. 12e) and SOE-sealed coating (Fig. 12f) after the same exposure duration. After 2000 h immersion, 83% of the excess sealant is stripped off from the surface of the BE-sealed coating (Fig. 12g). This illustrates that the corrosive media penetrates the surface of the sealed layer and BE-sealed coating through the microdefects of the blank epoxy sealant (Ref 48), and the reduction in adhesion between the two results in the peeling off of the surface sealed layer. It should be noted that no sign of corrosion spot is observed on the surface of the SOE-sealed coating even after 2000 h exposure (Fig. 12h), indicating that it provides the best corrosion protection ability.

3.9 The Self-Healing Ability

The self-healing abilities of the BE and OE coatings with artificial defects are evaluated to assess the corrosion inhibition performance of MBI on steel substrate beneath the Fe-based AMC (Ref 24, 34). Note that the removal of the Fe-based AMC does not affect the experimental results. This is because the corrosive media diffuses into the interface of the Fe-based AMC and substrate through the coating defects, which is one of the most commonly encountered failure types (Ref 4, 10), and the Fe-based AMC acts as a cathode with respect to the substrate. The artificial defects permit quick and direct contact of the corrosive media with the substrate.

Figures 13 and 14 display the morphologies and elemental distributions of the coatings with scratches after 6 h immersion in 3.5 wt.% NaCl solution. As demonstrated by the elemental map, the white color represents the region with high concentration of C, Fe or O elements in the BE coating and the region with high concentration of O, Cl or S elements in the OE coating, respectively, while the blue color is the region with low concentration. Obvious corrosion products are observed inside
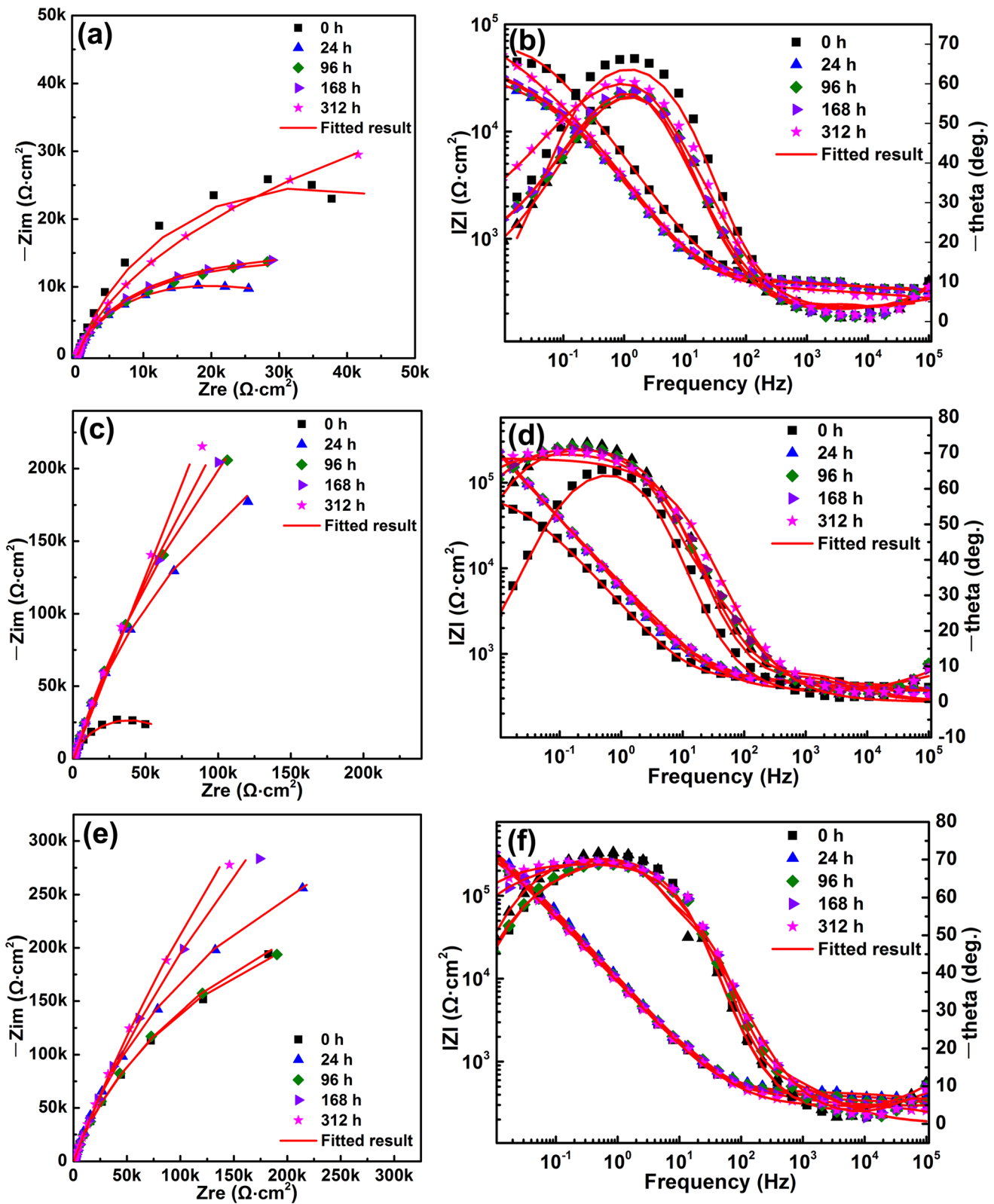
Fig. 8 Nyquist and Bode plots of the (a), (b) unsealed coating, (c), (d) BE-sealed coating, and (e), (f) OE-sealed coating immersed in 0.35 wt.% NaCl solution at different times

the scratched region of the BE coating (Fig. 13a) and the C signal is also absent (Fig. 13b). Moreover, the concentration of O element is observed to be higher inside the scratch than in any other area (Fig. 13d), suggesting that corrosion reaction

occurs in the scratch of the BE coating. Comparatively, there are only small amounts of corrosion products in the scratched area of the OE coating with most parts of the scratched area remaining clear (Fig. 14a). The O content in the scratch
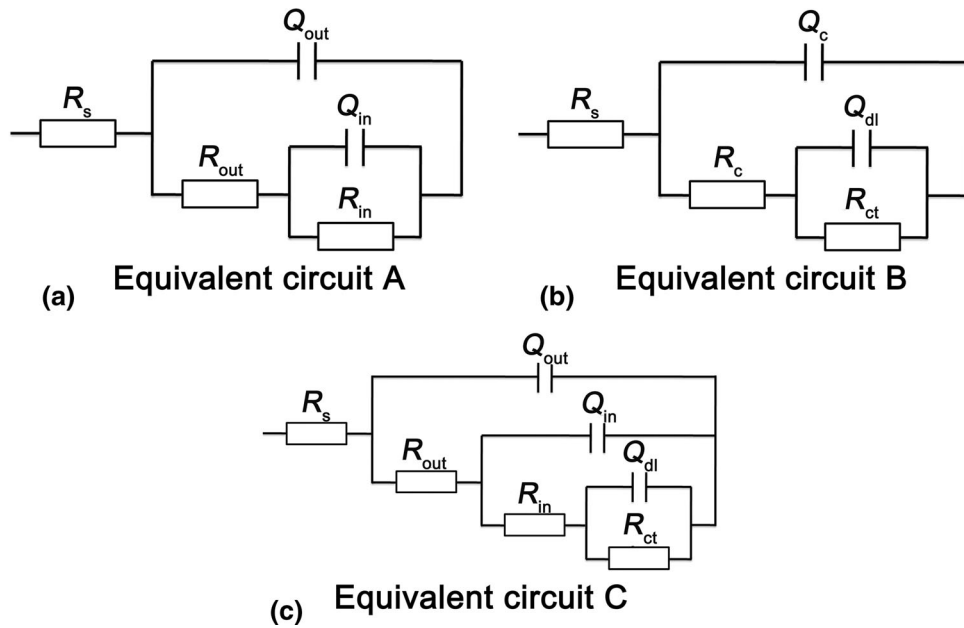
Fig. 9 Equivalent circuit models used to fit the EIS plots. Equivalent circuits A and B with two time constants are used for fitting the 0-24 h EIS data of the unsealed coating and sealed coatings, respectively, and Equivalent circuit C is used for fitting the 96-216 h EIS data of the three coatings
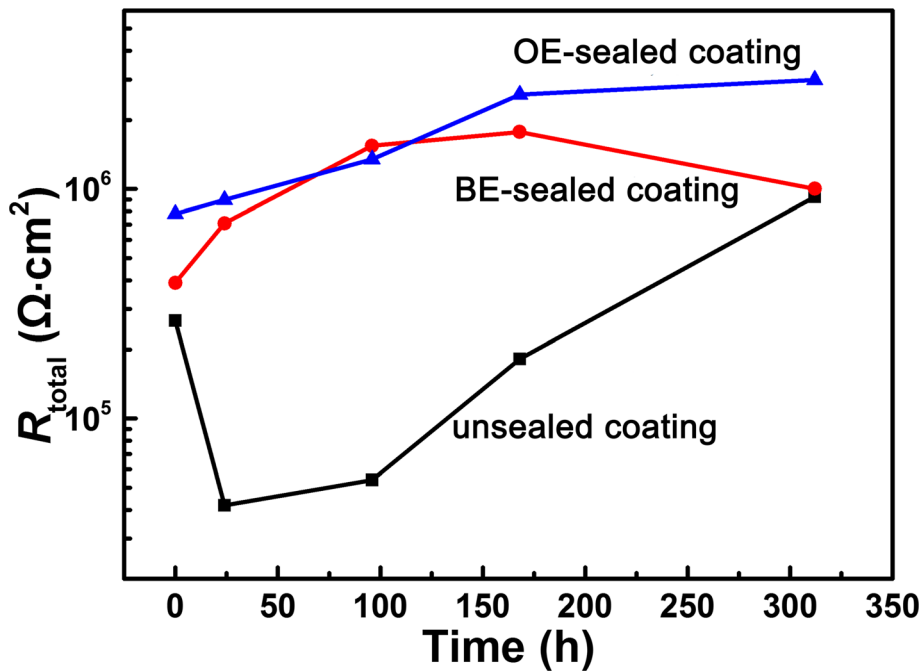

Fig. 10 Variation of R_{total} for the unsealed, BE-sealed and OE-sealed coatings with immersion time in 0.35 wt.% NaCl solution

(Fig. 14b) is considerably lower than that of the scratch on the BE coating (Fig. 13d). Furthermore, a new S element from MBI is detected on the scratch area (Fig. 14d), signifying that MBI is leached from the OMMT interlayer and adsorbs on the substrate surface to prevent the propagation of corrosion process. Therefore, the addition of OMMT to the epoxy sealant provides corrosion inhibition properties to the OE-sealed coating.
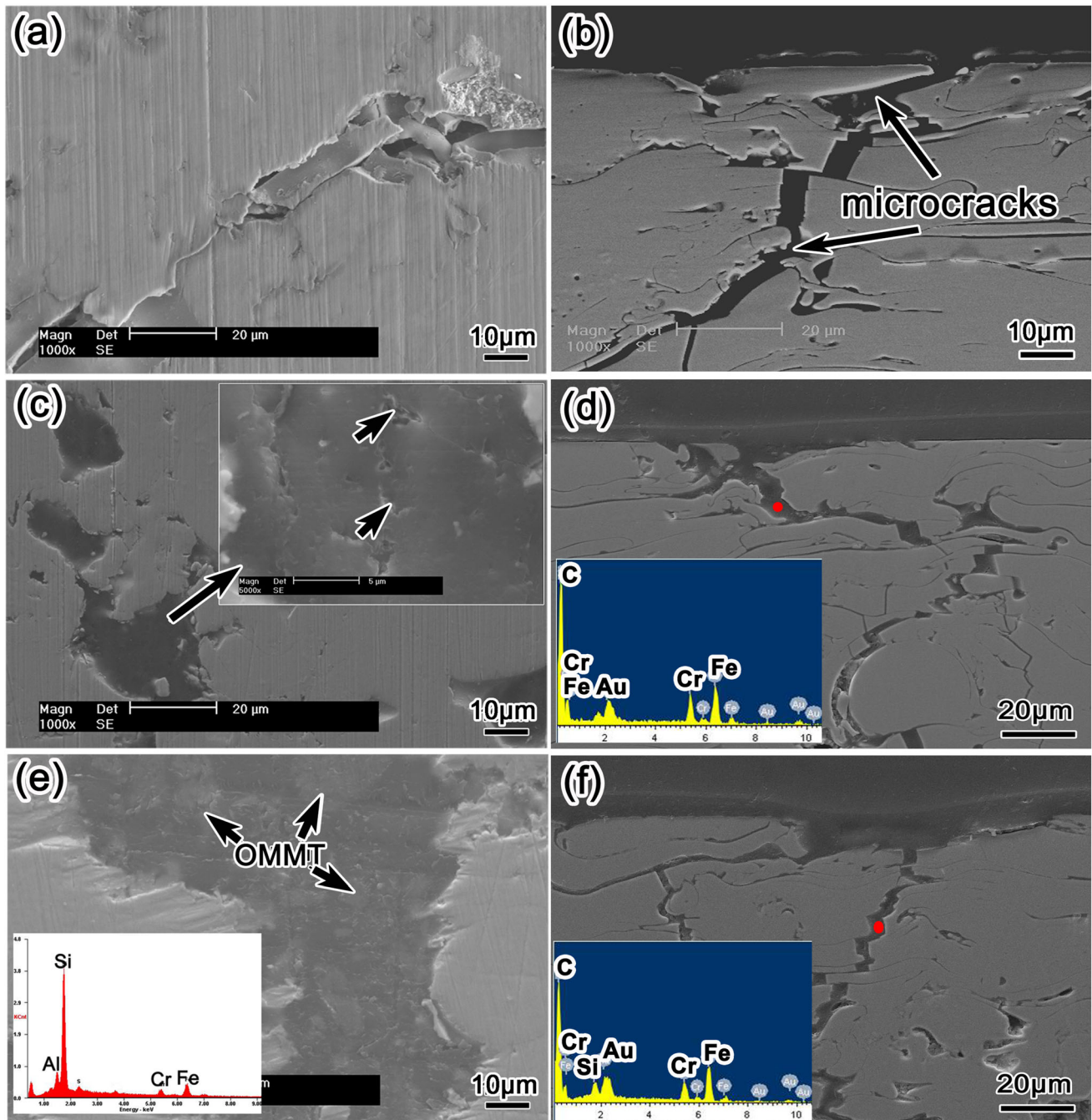
Fig. 11 The surface and cross-sectional morphologies of the (a), (b) unsealed coating, (c), (d) BE-sealed coating and (e), (f) OE-sealed coating

3.9.1 Corrosion Protection Mechanism. Structural defects, such as pores and cracks, in the unsealed coating (Fig. 11a and b) provide diffusion channels for the electrolyte to reach the steel substrate beneath the Fe-based AMC. With the coating as a large cathode and the substrate as a small anode, galvanic corrosion takes place (Ref 4, 46), and this enhances the dissolution of the substrate. As shown in Fig. 12a and d, corrosion products are observed on the surface of the Fe-based AMC. For the BE-sealed coating, the reduction of coating defects by epoxy sealing obstructs the diffusion

pathways of the corrosive media (Fig. 11c and d) and improves the corrosion performance of the coating (Fig. 8c and d), and this is in agreement with the works of Wu et al. (Ref 9), Gil et al. (Ref 14), etc. However, the blank epoxy sealed layer is susceptible to the penetration of the corrosive media with prolonged immersion (Ref 15-17). Some researchers pointed out that in some cases the number of corrosive species, such as dissolved oxygen, spreading beneath the blank organic coating was several times more than the minimum amount initiating the substrate corrosion (Ref 49). Ultimately, the BE-sealed coating
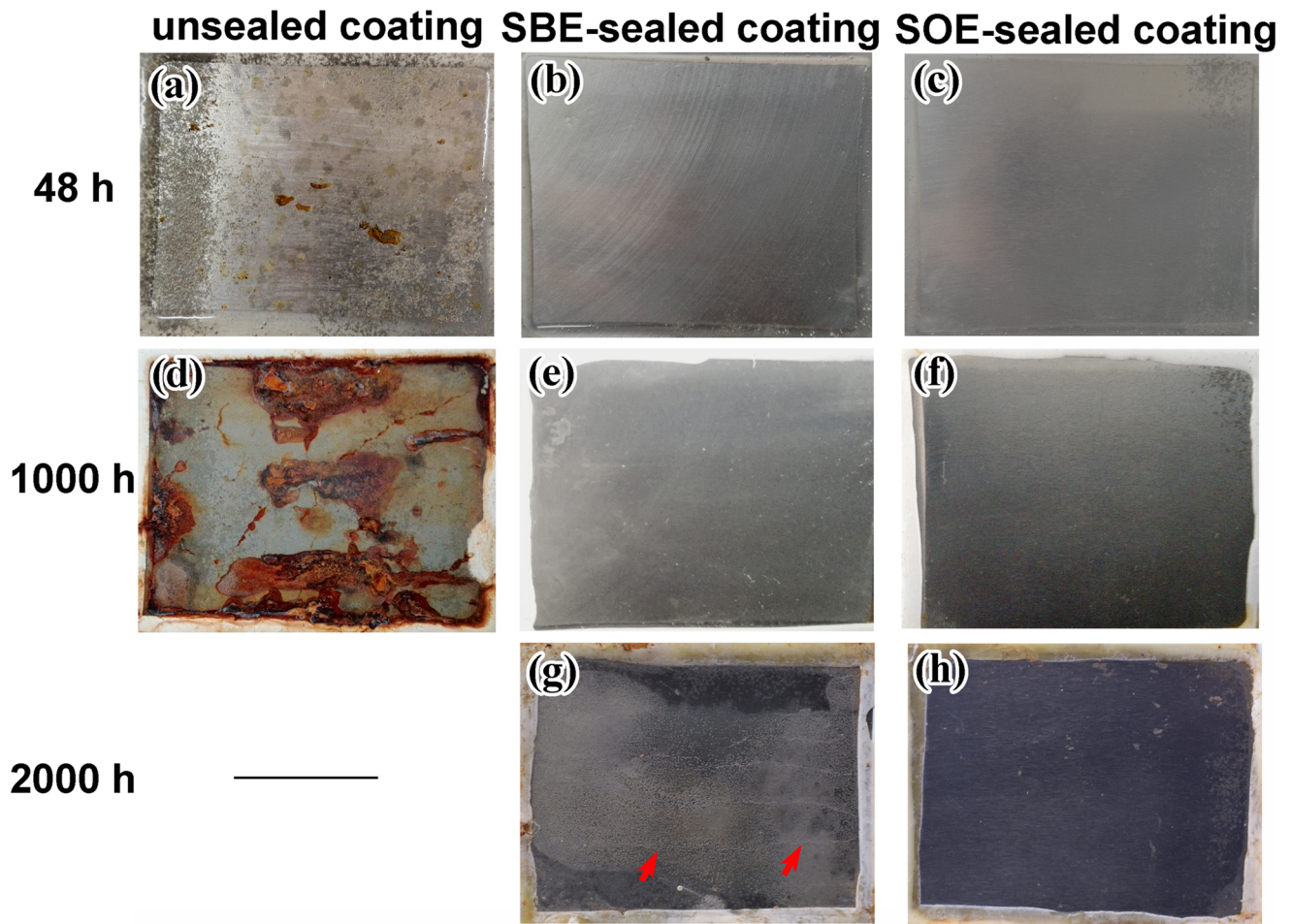
unsealed coating   SBE-sealed coating   SOE-sealed coating

48 h

1000 h

2000 h

Fig. 12 Optical images of the unsealed, SBE-sealed, and SOE-sealed coatings after exposures at varying times in the salt spray test. The excess sealants on the BE-sealed (SBE-sealed) and OE-sealed (SOE-sealed) coatings surface are not removed

is ineffective against corrosion. As seen in Figs. 10 and 12(g), the R_{total} decreases after 168 h immersion, and the sealed surface layer is peeled off from the BE-sealed coating.

In comparison, the OE-sealed coating displays the best corrosion performance, and some mechanisms that could account for its superior corrosion resistance are listed as follows:

(1) The shielding effect of the epoxy sealant loaded with OMMT

Due to the ion exchange and swelling of MT, protonated octadecylamine ($CH_3(CH_2)_{17}NH_3^+$) can be exchanged with the cations within the MT interlayer. The possible reaction can be expressed as Eq 4, where m represents the cations present in the MT gallery.

$$m - MT + CH_3(CH_2)_{17}NH_3^+ \rightleftharpoons CH_3(CH_2)_{17}NH_3 - MT + m^+$$

(Eq 4)
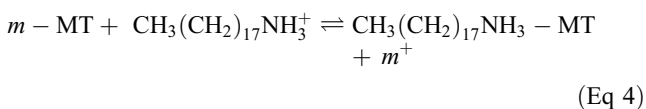
The length of the octadecylamine molecule is about 23.97 Å, which is larger than those of the cations between the MT interlayer. Therefore, the successful incorporation of octadecylamine into MT (MMT) directly results in an increase

in the interlayer spacing from 1.245 to 1.846 nm (Fig. 5). Moreover, the increased basal spacing of MMT favors the loading of MBI with a length of about 8.67 Å and a width of about 5.34 Å (OMMT). As demonstrated by FTIR (Fig. 3) and TGA (Fig. 4), both octadecylamine and MBI are successfully intercalated into the OMMT interlayer. The results of SEM (Fig. 2) and XRD (Fig. 5) reveal that the layer spacing of OMMT is larger and presents a thin-layer structure. Additionally, after the two-step treatment, the polarity of MT changes from hydrophilic to hydrophobic. As described in Fig. 1, OMMT is relatively soluble in ethanol, and similarly, it exhibits good compatibility with the organic epoxy sealant. Also, with its thin layer structure, the OMMT is uniformly and stably dispersed in the epoxy sealant, which can improve the shielding performance of the sealed layer and effectively reduce the diffusion path of the corrosive media (Fig. 15a). Thus, the corrosion resistance of the OE-sealed coating is improved.

(2) The inhibition role of MBI released from the OMMT interlayer.

With the transport of aggressive media to the substrate beneath the OE-sealed coating, the occurrence of anodic and cathodic reactions leads to the change of local pH values. The pH altering triggers the release of MBI from the OMMT interlayer,
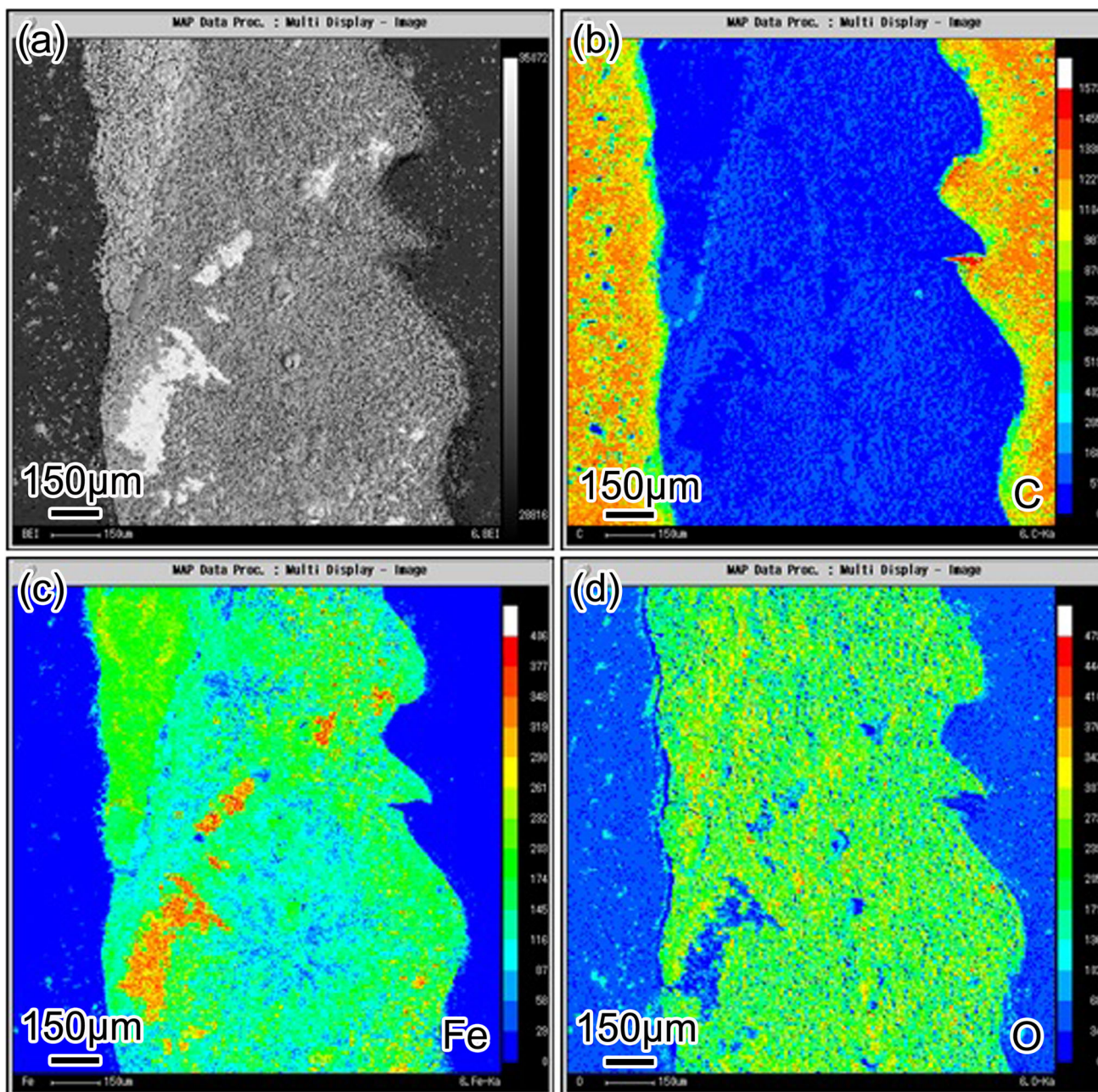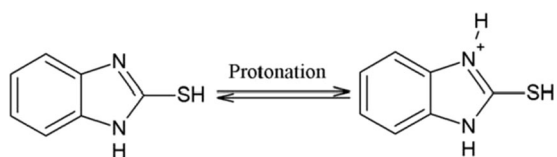
Fig. 13 EPMA mapping of the scratched region of the BE coating immersed in 3.5 wt.% NaCl solution for 6 h. (a) Backscattered electron image; The distribution of (b) C element, (c) Fe element and (d) O element. BE coating: The substrate is directly sealed with blank epoxy, except for Fe-based AMC

and the released MBI exists in protonated and deprotonated forms (Eq 5, 6) (Ref 24, 50, 51). As observed in Fig. 7, the corrosion inhibitor (MBI) in the OMMT interlayer is released, and the released amount counteracts the effect of the corrosive media. Also, the presence of the S element within the scratched region of the OE coating confirms the release of MBI from the OMMT interlayer. Then, the leached MBI is adsorbed on the active anodic sites (Fig. 15b), and reacts with the dissolved Fe^{2+} (Eq 7) to form insoluble compounds against corrosion (Fig. 15c) (Ref 24, 51-53). The corresponding corrosion protection mechanism is illustrated in Fig. 15.
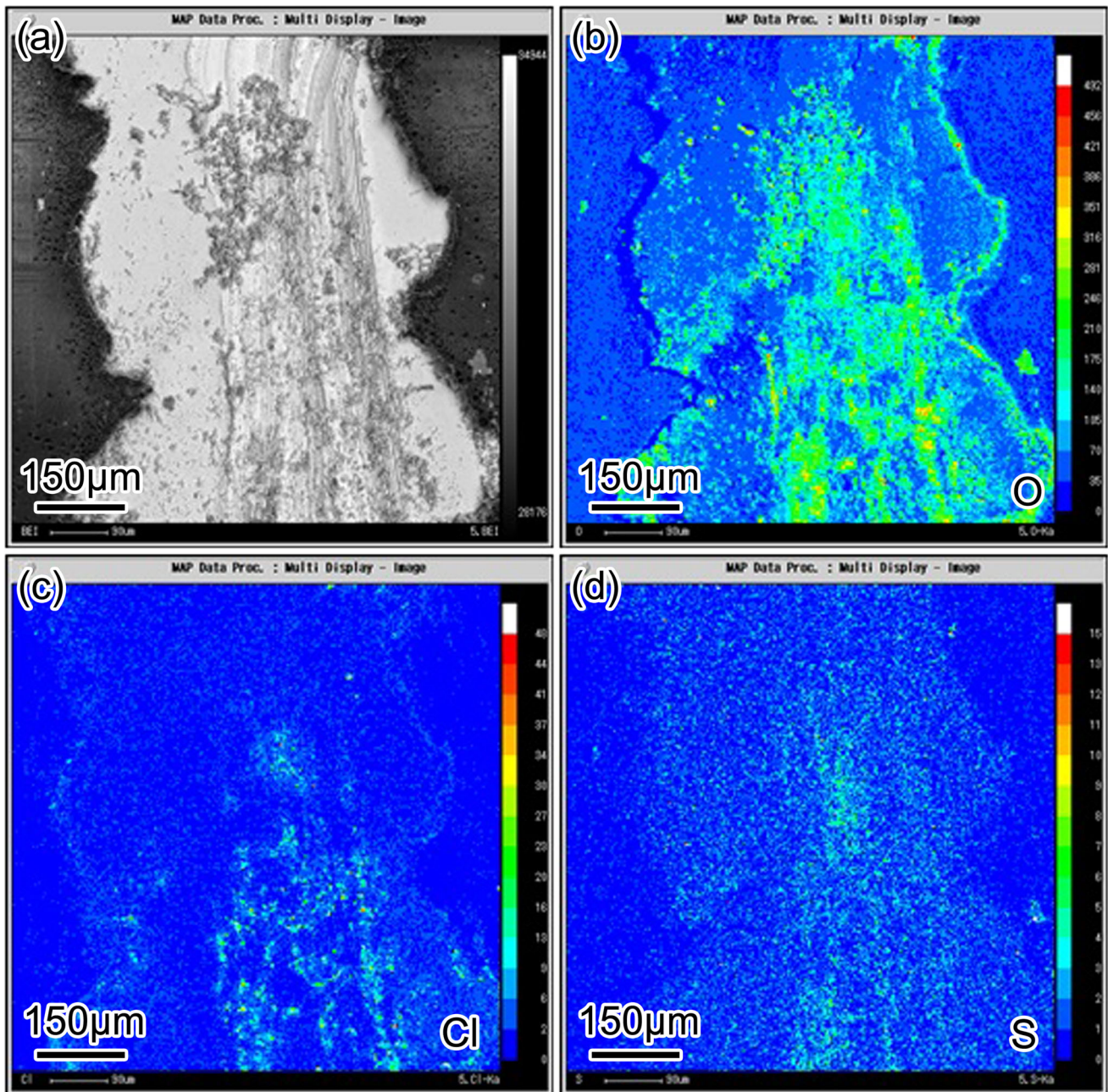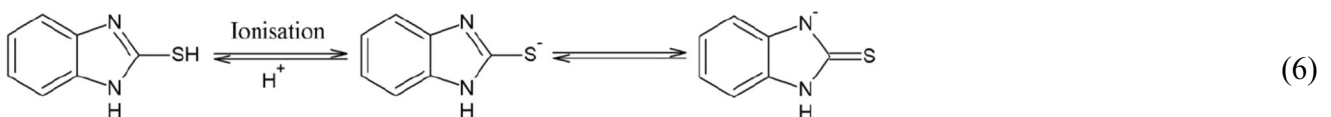

$$(5)$$

Fig. 14 EPMA mapping of the scratched region of the OE coating immersed in 3.5 wt.% NaCl solution for 6 h. (a) Backscattered electron image; The distribution of (b) O element, (c) Cl element and (d) S element. OE coating: The substrate is directly sealed with OMMT-loaded epoxy, except for Fe-based AMC
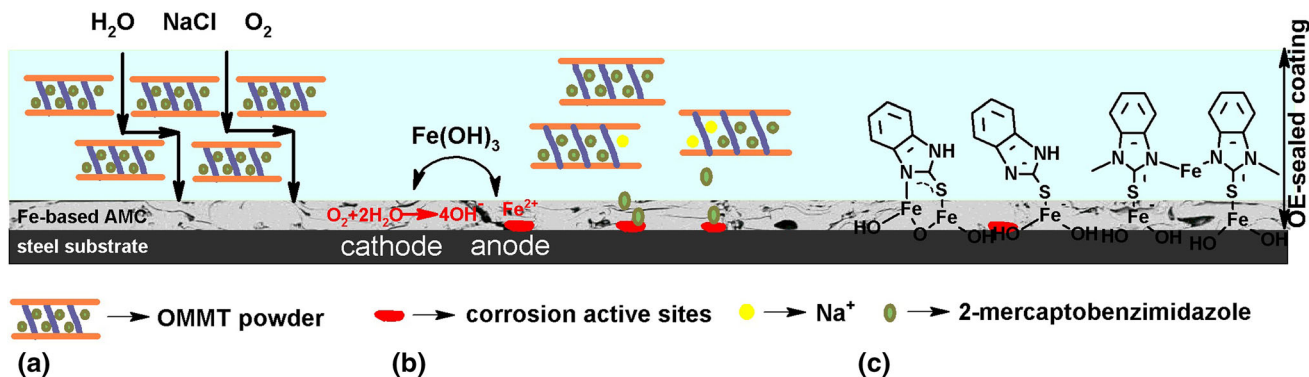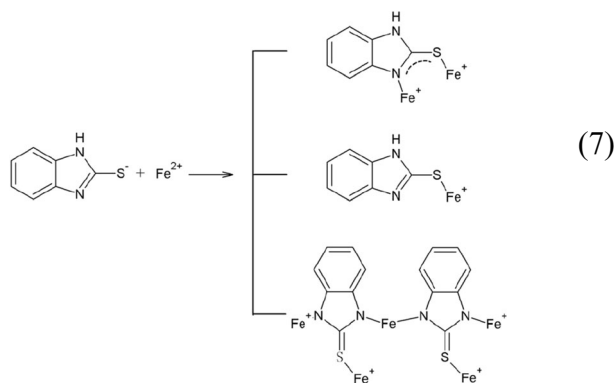

(6)

Fig. 15 Schematic representation of the corrosion protection mechanism of the OE-sealed coating. (a) the shielding performance of the epoxy sealant loaded with OMMT; (b) the release of MBI from the OMMT interlayer; (c) the corrosion inhibition role of MBI on the OE-sealed coating

$$(7)$$

Mahdavian et al. (Ref 51) reported that the presence of nitrogen and sulfur atoms in MBI was responsible for the high adsorption ability of the azole compounds on steel surface, hence the strong corrosion inhibition effect of MBI. As shown in Fig. 14, the corrosion phenomenon of the OE coating is obviously reduced relative to that of the BE coating. Moreover, the ionized MBI (Eq. 6) with high adsorption capacity exhibits competitive adsorption with the corrosive ions (Ref 50, 52, 53), which decreases the anodic area, and thus the corrosion rate of the substrate.

According to the above analysis, it can be concluded that the OE-sealed coating displays superior corrosion resistance compared with the other two coatings, and this is consistent with the results of the EIS (Figs. 8 and 10) and salt spray test (Fig. 12).

4. Conclusions

Octadecylamine and 2-mercaptobenzimidazole are successfully intercalated into the interlayer of MT, and this causes the expansion of the basal spacing for OMMT with a single layer of slices. UV result shows the release possibility of the MBI inside the OMMT interlayer, and the exchangeability is related to the corrosive media. The structural defects of the Fe-based AMC are reduced after sealing treatments, and based on EIS and salt spray test results, the corrosion resistance of the coatings follows the order: OE-sealed coating > BE-sealed coating > unsealed coating. Consequently, two reasons are proposed for the superior corrosion resistance of the OE-sealed

coating. Firstly, with its thin layer structure, the uniform dispersion of OMMT in the epoxy sealant provides high shielding performance for the OE-sealed coating against the penetration of corrosive media. Secondly, the MBI released from the OMMT interlayer is adsorbed on the corrosion sites and provides active corrosion protection.

References

1. C. Suryanarayana and A. Inoue, Iron-Based Bulk Metallic Glasses, *Int. Mater. Rev.*, 2013, **58**(3), p 131–166.
2. A. Inoue and A. Takeuchi, Recent Development and Application Products of Bulk Glassy Alloys, *Acta Mater.*, 2011, **59**, p 2243–2267.
3. S.D. Zhang, W.L. Zhang, S.G. Wang, X.J. Gu, and J.Q. Wang, Characterisation of Three-Dimensional Porosity in an Fe-Based Amorphous Coating and its Correlation with Corrosion Behaviour, *Corros. Sci.*, 2015, **93**, p 211–221.
4. S.D. Zhang, J. Wu, W.B. Qi, and J.Q. Wang, Effect of Porosity Defects on the Long-Term Corrosion Behaviour of Fe-Based Amorphous Alloy Coated Mild Steel, *Corros. Sci.*, 2016, **110**, p 57–70.
5. J. Huang, D.C. Zhao, Y. Gong, C. Yang, H.Y. Zhu, M.L. Wang, D. Chen, and H.W. Wang, Improved Corrosion Resistance of PEO-Coated 7085Al Alloy via a Novel Organic and Inorganic Sealing-Treatment Combination, *Surf. Coat. Technol.*, 2022, **441**, p 128566.
6. G.M. Qin, Y.C. Zhang, E.H. Yang, Z.W. Peng, W. Wei, X.M. Xie, and W.Z. Li, Effect of Post-Sealing Treatment with Different Concentrations of NaH_2PO_4 on Corrosion Resistance of MAO Coating on 6063 Aluminum Alloy, *Surf. Coat. Technol.*, 2022, **443**, p 128604.
7. L. Yang, X.H. Shi, X.F. Tian, X. Han, J.R. Mu, and L.H. Qi, Effect of Sealing Treatment on Corrosion Behavior of Plasma Sprayed ZrO_2 Coated C_f/Mg Composites, *Surf. Coat. Technol.*, 2021, **423**, p 127627.
8. M.M. Liu, H.X. Hu, Y.G. Zheng, J.Q. Wang, Z.H. Gan, and S. Qiu, Effect of Sol–Gel Sealing Treatment Loaded with Different Cerium Salts on the Corrosion Resistance of Fe-Based Amorphous Coating, *Surf. Coat. Technol.*, 2019, **367**, p 311–326.
9. J. Wu, S.D. Zhang, W.H. Sun, Y. Gao, and J.Q. Wang, Enhanced Corrosion Resistance in Fe-Based Amorphous Coatings through Eliminating Cr-Depleted Zones, *Corros. Sci.*, 2018, **136**, p 161–173.
10. J. Wu, S.D. Zhang, W.H. Sun, and J.Q. Wang, Influence of Oxidation Related Structural Defects on Localized Corrosion in HVAF-Sprayed Fe-Based Metallic Coatings, *Surf. Coat. Technol.*, 2018, **335**, p 205–218.

11. J. Jiao, Q. Luo, X.S. Wei, Y. Wang, and J. Shen, Influence of Sealing Treatment on the Corrosion Resistance of Fe-Based Amorphous Coatings in HCl Solution, *J. Alloy. Compd.*, 2017, **714**, p 356–362.

12. M.M. Liu, H.X. Hu, and Y.G. Zheng, Effects of Three Sealing Methods of Aluminum Phosphate Sealant on Corrosion Resistance of the Fe-Based Amorphous Coating, *Surf. Coat. Technol.*, 2017, **309**, p 579–589.

13. Y. Wang, S.L. Jiang, Y.G. Zheng, W. Ke, W.H. Sun, and J.Q. Wang, Effect of porosity Sealing Treatments on the Corrosion Resistance of High-Velocity Oxy-Fuel (HVOF)-Sprayed Fe-based Amorphous Metallic Coatings, *Surf. Coat. Technol.*, 2011, **206**, p 1307–1318.

14. S. Liscano, L. Gil, and M.H. Staia, Effect of Sealing Treatment on the Corrosion Resistance of Thermal-Sprayed Ceramic Coatings, *Surf. Coat. Technol.*, 2004, **188–189**, p 135–139.

15. Y. González-García, S. González, and R.M. Souto, Electrochemical and Structural Properties of a Polyurethane Coating on Steel Substrates for Corrosion Protection, *Corros. Sci.*, 2007, **49**, p 3514–3526.

16. S. González, I.C. Mirza Rosca, and R.M. Souto, Investigation of the Corrosion Resistance Characteristics of Pigments in Alkyd Coatings on Steel, *Prog. Org. Coat.*, 2001, **43**, p 282–285.

17. E.P.M. van Westing, G.M. Ferrari, and J.H.W. de Wit, The Determination of Coating Performance with Impedance Measurements-I. Coating Polymer Properties, *Corros. Sci*, 1993, **34**, p 1511–1530.

18. Y.X. Chen, W.B. Bai, J.P. Chen, X.Y. Chen, J. Zhao, and F.F. Wei, In-Situ Intercalation of Montmorillonite/urushiol Titanium Polymer Nanocomposite for Anti-Corrosion and Anti-Aging of Epoxy Coatings, *Prog. Org. Coat.*, 2022, **165**, p 106738.

19. N. Soltani, H. Salavati, and A. Moghadasi, The Role of Na-Montmorillonite/Cobalt Ferrite Nanoparticles in the Corrosion of Epoxy Coated AA 3105 Aluminum Alloy, *Surf. Interfaces*, 2019, **15**, p 89–99.

20. V. Dalmoro, J.H. dos Santos, E. Armelin, C. Alemán, and D.S. Azambuja, Sol-Gel Hybrid Films Based on Organosilane and Montmorillonite for Corrosion Inhibition of AA2024, *J. Colloid Interface Sci.*, 2014, **426**, p 308–313.

21. N.V. Phuong, B.R. Fazal, and S. Moon, Cerium- and Phosphate-Based Sealing Treatments of PEO Coated AZ31 Mg Alloy, *Surf. Coat. Technol.*, 2017, **309**, p 86–95.

22. M. Mohedano, C. Blawert, and M.L. Zheludkevich, Cerium-Based Sealing of PEO Coated AM50 Magnesium Alloy, *Surf. Coat. Technol.*, 2015, **269**, p 145–154.

23. M. Laleh, F. Kargar, and A.S. Rouhaghdam, Investigation of Rare Earth Sealing of Porous Micro-Arc Oxidation Coating Formed on AZ91D Magnesium Alloy, *J. Rare Earth*, 2012, **30**(11), p 1293–1297.

24. S.A. Haddadi, A. Ramazani S.A., M. Mahdavian, and M. Arjmand, Epoxy Nanocomposite Coatings with Enhanced Dual Active/Barrier Behavior Containing Graphene-Based Carbon Hollow Spheres as Corrosion Inhibitor Nanoreservoirs, *Corros. Sci.*, 2021, **185**, p 1–17.

25. R. Behgam, M. Mahdavian, and A. Ramazani, Fabrication of Hollow Carbon Spheres Doped with Zinc Cations to Enhance Corrosion Protection of Organosilane Coatings, *Surf. Interfaces*, 2020, **21**, p 100696.

26. I. Mohammadi, M. Izadi, T. Shahrabi, D. Fathi, and A. Fateh, Enhanced Epoxy Coating Based on Cerium Loaded Na-Montmorillonite as Active Anti-Corrosive Nanoreservoirs for Corrosion Protection of Mild Steel: Synthesis, Characterization, and Electrochemical Behavior, *Prog. Org. Coat.*, 2019, **131**, p 119–130.

27. S.A. Haddadi, A. Ramazani S.A., M. Mahdavian, P. Taheri, J.M.C. Mol, and Y. Gonzalez-Garcia, Self-Healing Epoxy Nanocomposite Coatings based on Dual-Encapsulation of Nano-Carbon Hollow Spheres with Film-Forming Resin and Curing Agent, *Compos. Part B: Eng.*, 2019, **175**, p 107087.

28. Y. Morozov, L.M. Calado, R.A. Shakoor, R. Raj, R. Kahraman, M.G. Taryba, and M.F. Montemor, Epoxy Coatings Modified with a new Cerium Phosphate Inhibitor for Smart Corrosion Protection of Steel, *Corros. Sci.*, 2019, **159**, p 1–12.

29. M. Kaseem and Y.G. Ko, Benzoate Intercalated Mg-Al-Layered Double Hydroxides (LDHs) as Efficient Chloride Traps for Plasma Electrolysis Coatings, *J. Alloy. Compd.*, 2019, **787**, p 772–778.

30. X. Zhang, F. Zhong, X. Li, B. Liu, C. Zhang, B. Buhe, T. Zhang, G. Meng, and F. Wang, The Effect of Hot Extrusion on the Microstructure and Anti-Corrosion Performance of LDHs Conversion Coating on AZ91D Magnesium Alloy, *J. Alloy. Compd.*, 2019, **788**, p 756–767.

31. M. Izadi, T. Shahrabi, and B. Ramezanzadeh, Active Corrosion Protection Performance of an Epoxy Coating Applied on the Mild Steel Modified with an Eco-Friendly Sol-Gel Film Impregnated with Green Corrosion Inhibitor Loaded Nanocontainers, *Appl. Surf. Sci.*, 2018, **440**, p 491–505.

32. E. Alibakhshi, E. Ghasemi, M. Mahdavian, and B. Ramezanzadeh, A comparative Study on Corrosion Inhibitive Effect of Nitrate and Phosphate Intercalated Zn-Al-Layered Double Hydroxides (LDHs) Nanocontainers Incorporated into a Hybrid Silane Layer and their Effect on Cathodic Delamination of Epoxy Topcoat, *Corros. Sci.*, 2017, **115**, p 159–174.

33. S.H. Adsul, T. Siva, S. Sathiyanarayanan, S.H. Sonawane, and R. Subasri, Aluminum Pillared Montmorillonite Clay-Based Self-Healing Coatings for Corrosion Protection of Magnesium Alloy AZ91D, *Surf. Coat. Technol.*, 2018, **352**, p 445–461.

34. A. Ghazi, E. Ghasemi, M. Mahdavian, B. Ramezanzadeh, and M. Rostami, The Application of Benzimidazole and Zinc Cations Intercalated Sodium Montmorillonite as Smart Ion Exchange Inhibiting Pigments in the Epoxy Ester Coating, *Corros. Sci.*, 2015, **94**, p 207–217.

35. M.M. Liu, Z.B. Wang, H.X. Hu, L.M. Zhang, and Y.G. Zheng, Effect of Sealing Treatments on Erosion-Corrosion of a Fe-Based Amorphous Metallic Coating in 3.5 wt.% NaCl Solution with 2 wt.% Sand, *Metals-Basel*, 2022, **12**, p 680.

36. Z.B. Zheng, Y.G. Zheng, W.H. Sun, and J.Q. Wang, Effect of Heat Treatment on the Structure, Cavitation Erosion and Erosion–Corrosion Behavior of Fe-Based Amorphous Coatings, *Tribol. Int.*, 2015, **90**, p 393–403.

37. I.A. Siddiquey, E. Ukaji, T. Furusawa, M. Sato, and N. Suzuki, The Effects of Organic Surface Treatment by Methacryloxypropyltrimethoxysilane on the Photostability of TiO₂, *Mater. Chem. Phys.*, 2007, **105**, p 162–168.

38. A. Alemdar, N. Gungor, O.I. Ece, and O. Atici, The Rheological Properties and Characterization of Bentonite Dispersions in the Presence of Non-Ionic Polymer PEG, *J. Mater. Sci.*, 2005, **40**, p 171–177.

39. H. Chen, Y. Li, S. Wang, and Y. Zhou, Synthesis of Montmorillonite/Fe₃O₄-OTAB Composite Capable of using as Anisotropic Nanoparticles, *Appl. Surf. Sci.*, 2017, **402**, p 384–391.

40. M. Sabzi, S.M. Mirabedini, J. Zohuriaan-Mehr, and M. Atai, Surface Modification of TiO₂ Nano-Particles with Silane Coupling Agent and Investigation of its Effect on the Properties of Polyurethane Composite Coating, *Prog. Org. Coat.*, 2009, **65**, p 222–228.

41. A. Barth, Review the Infrared Absorption of Amino Acid Side Chains, *Prog. Biophys. Mol. Bio.*, 2000, **74**, p 141–173.

42. N. B. Colthup, L. H. Daly, and S. E. Wiberley, *Introduction to Infrared and Raman Spectroscopy (Second Edition)*, Academic Press, INC., New York, 1975.

43. B. Gong, P. Wu, Z. Huang, Y. Li, S. Yang, Z. Dang, B. Ruan, and C. Kang, Efficient Inhibition of Heavy Metal Release from Mine Tailings Against Acid Rain Exposure by Triethylenetetramine Intercalated Montmorillonite (TETA-Mt), *J. Hazard. Mater.*, 2016, **318**, p 396–406.

44. F. Liu, E.-H. Han, W. Ke, N. Tang, J. Wan, G. Yin, J. Deng, and K. Zhao, Polar Influence of the Organic Modifiers on the Structure of Montmorillonite in Epoxy Nanocomposites, *J. Mater. Sci. Technol.*, 2013, **29**(11), p 1040–1046.

45. B. Mingo, R. Arrabal, M. Mohedano, Y. Llamazares, E. Matykina, A. Yerokhin, and A. Pardo, Influence of Sealing Post-Treatments on the Corrosion Resistance of PEO Coated AZ91 Magnesium Alloy, *Appl. Surf. Sci.*, 2018, **433**, p 653–667.

46. J. Creus, H. Mazille, and H. Idrissi, Porosity Evaluation of Protective Coatings onto Steel, through Electrochemical Techniques, *Surf. Coat. Technol.*, 2000, **130**, p 224–232.

47. Z. Liu, D. Yan, Y. Dong, Y. Yang, Z. Chu, and Z. Zhang, The Effect of Modified Epoxy Sealing on the Electrochemical Corrosion Behaviour of Reactive Plasma-Sprayed TiN Coatings, *Corros. Sci.*, 2013, **75**, p 220–227.

48. Y. Hao, F. Liu, and E.-H. Han, Mechanical and Barrier Properties of Epoxy/Ultra-Short Glass Fibers Composite Coatings, *J. Mater. Sci. Technol.*, 2012, **28**(12), p 1077–1084.

49. M. Behzadnasab, S.M. Mirabedini, and M. Esfandeh, Corrosion Protection of Steel by Epoxy Nanocomposite Coatings Containing Various Combinations of Clay and Nanoparticulate Zirconia, *Corros. Sci.*, 2013, **75**, p 134–141.

50. M. Finšgar, 2-Mercaptobenzimidazole as a Copper Corrosion Inhibitor: Part II Surface Analysis Using X-ray Photoelectron Spectroscopy, *Corros. Sci.*, 2013, **72**, p 90–98.

51. M. Mahdavian and S. Ashhari, Corrosion Inhibition Performance of 2-Mercaptobenzimidazole and 2-Mercaptobenzoxazole Compounds for Protection of Mild Steel in Hydrochloric Acid Solution, *Electrochim. Acta*, 2010, **55**, p 1720–1724.

52. J. Aljourani, K. Raeissi, and M.A. Golozar, Benzimidazole and its Derivatives as Corrosion Inhibitors for Mild Steel in 1M HCl Solution, *Corros. Sci.*, 2009, **51**, p 1836–1843.

53. H. Amar, A. Tounsi, A. Makayssi, A. Derja, J. Benzakour, and A. Outzourhit, Corrosion Inhibition of Armco Iron by 2-Mercaptobenz-imidazole in Sodium Chloride 3% Media, *Corros. Sci.*, 2007, **49**, p 2936–2945.